AGU ADVANCING EARTH AND SPACE SCIENCES

AGU Advances

RESEARCH ARTICLE
10.1029/2025AV002097

Widespread Impact-Induced Crustal Permeability on the Early Earth

A. M. Alexander[1], **S. Marchi**[1], and **B. C. Johnson**[2,3]

[1]Southwest Research Institute, Boulder, CO, USA, [2]Department of Earth, Atmospheric and Planetary Sciences, Purdue University, West Lafayette, IN, USA, [3]Department of Physics and Astronomy, Purdue University, West Lafayette, IN, USA

Peer Review The peer review history for this article is available as a PDF in the Supporting Information.

Key Points:

- Vast permeable regions were generated in the upper crust by impact-generated fracturing in the Hadean and Archean
- The volume of impact-induced permeable regions is strongly dependent on impact energy
- Crustal permeable networks generated by recursive impacts during the Hadean and early Archean may have served as vestiges for early life

Supporting Information:

Supporting Information may be found in the online version of this article.

Correspondence to:

A. M. Alexander,
amanda.alexander@swri.org

Citation:

Alexander, A. M., Marchi, S., & Johnson, B. C. (2026). Widespread impact-induced crustal permeability on the early Earth. *AGU Advances*, *7*, e2025AV002097. https://doi.org/10.1029/2025AV002097

Received 22 SEP 2025
Accepted 16 APR 2026

Author Contributions:

Conceptualization: S. Marchi
Formal analysis: A. M. Alexander
Funding acquisition: S. Marchi
Methodology: A. M. Alexander
Software: A. M. Alexander, B. C. Johnson
Supervision: S. Marchi, B. C. Johnson
Validation: S. Marchi, B. C. Johnson
Visualization: A. M. Alexander
Writing – original draft: A. M. Alexander
Writing – review & editing: A. M. Alexander, S. Marchi, B. C. Johnson

Abstract The early Earth (i.e., Archean and Hadean Eons, 2.5–4.0 and 4.0–4.5 Ga, respectively) experienced frequent cosmic bombardment. Impacts have been shown to stimulate crustal alteration, for instance via hydrothermal systems active for up to millions of years post-impact. Using a shock physics code that includes the effects of tensile fragmentation and porosity generation, we conduct the first comprehensive study to quantify impact-generated permeable volumes into the upper crust of the early Earth for a suite of environmental (e.g., geothermal gradient, crustal thickness, presence of an ocean) and impact conditions (e.g., impactor velocity and size). Inferences from our suite of impact simulations suggest that the volume of impact-induced permeable regions is strongly dependent on impact energy (i.e., impactor size and velocity). The range of generated permeability (10^{-20} to 10^{-12} m^2) within those regions, however, depends on the geothermal gradient and crustal composition. Moreover, we use a bombardment history model to infer the cumulative effects of recursive impacts onto the early Earth. We estimate that the upper 8 km shell of the Earth's crust may have been made highly permeable by impacts prior to 4.3 Ga, and that a significant portion of this volume would have been permeable until 3.5 Ga. These results show that impacts were instrumental in driving hydrothermal alteration of the early Earth's crust, with important consequences for the geochemical evolution of near-surface environments.

Plain Language Summary Asteroid impacts on Earth and Mars have been found to have generated hydrothermal systems. As a result of the impact, the crust is fractured. Heat from the impact and the background geothermal gradient of the Earth's interior then allows for fluid circulation through these fractures. Hydrothermal systems are thought to be environments in which life may have originated and/or evolved. Thus, it is important to understand and quantify the generation of these systems by impacts on the early Earth. In this study, we use computer models to simulate asteroid impacts of different sizes and velocities hitting the Earth. We also vary the conditions of the early Earth accounting for a warmer interior and different crustal compositions. When then calculate the volume of crust that is made permeable (i.e., fractured such that fluid can flow) by impacts for each case. Finally, we consider the frequency of impacts on the early Earth and then estimate how much volume of the Earth's upper crust would have been permeable throughout its first 1.5 billion years. The vast permeable regions generated by these impacts likely led to prolonged hydrothermal activity within the upper crust.

1. Introduction

Cosmic impacts were frequent on the early Earth. Impacts from planetesimals leftover from inner solar system accretion and asteroids shoved inward by dynamical perturbations hit the Earth at rates up to 10^5 more frequent than today (Marchi et al., 2009, 2014, 2021; Mojzsis et al., 2019; Nesvorný et al., 2023). The impact flux for this era (specifically the Archean, 2.5–4.0 Ga, and Hadean, 4.0–4.5 Ga) can be estimated from the lunar cratering record, radiometric ages of lunar samples, lunar and terrestrial highly-siderophile abundances, and from terrestrial spherule layers (Brasser et al., 2020; Johnson & Melosh, 2012; Johnson et al., 2016; Marchi et al., 2009, 2012, 2014, 2021; Morbidelli et al., 2012, 2018; Nesvorný et al., 2023; Neukum, 1984; Robbins, 2014).

As a result of a hypervelocity impact, a hemispheric shock wave expands into the subsurface followed closely thereafter by a rarefaction or release wave. The rarefaction puts material into tension as it passes and is capable of fragmenting large volumes of underlying rock. Chasmendolithic (fractures) and cryptoendolithic (internal porosities) environments have been observed at terrestrial impact structures (e.g., Cockell et al., 2005; Osinski et al., 2020). If the fractures and pores are interconnected, then fluid can flow. Fluid flow, coupled with heat from

the impact (from nearby impact melt rocks, elevated geothermal gradients in central uplifts, and energy deposited by passage of the shock wave), allows for the generation of hydrothermal fluid circulation (Cockell et al., 2024; Osinski et al., 2013, 2020). These hydrothermal environments can be active for millions of years, depending on the crater size (Abramov & Kring, 2005, 2007; Kirsimäe & Osinski, 2012; Kring et al., 2020; Marchi et al., 2024; Osinski et al., 2013; Trowbridge et al., 2024). Hydrothermal mineralization within impact structures has been observed on Earth and Mars (Kring et al., 2020; Osinski et al., 2013). Notably, hydrothermal systems are thought to be key environments for the origin and evolution of early life (e.g., Longo & Damer, 2020; Martin et al., 2008; Osinski et al., 2020). More generally, impacts have also been shown to create habitable environments conducive to microbial colonization (Osinski et al., 2020) in the form of lithophytic communities, hydrothermal systems, and impact crater lakes. Some of these environments are created within the subsurface, sometimes kilometers in depth, and provide protection from the potentially harsh environment at the surface.

Previous modeling efforts of the post-impact effects on the early Earth tend to focus on the thermal effects on habitability (e.g., Abramov & Kring, 2005; Abramov & Mojzsis, 2009; Abramov et al., 2013; Grimm & Marchi, 2018). Earlier studies modeling fluid flow in this era used now outdated assumptions about the impact flux (i.e., invoking a late heavy bombardment) or assume that impact-generated porosity and permeability decrease exponentially with depth— but recent studies have shown that porosity and permeability vary in complex ways both laterally and vertically in impact structures (Alexander et al., 2024; Marchi et al., 2024). Moreover, previous models did not take into account permeability due to fragmentation. Wiggins et al. (2022) suggested that the area of impact fractured rocks during the Hadean may have exceeded three times the surface area of the Earth. Such extensive fragmentation would have major implications for permeability (as was shown in Alexander et al., 2024), wherein the inclusion of fragmentation increased the permeable volume by an order of magnitude as compared to previous estimates and drill core data. Numerical modeling coupled with an analytical permeability computation which accounts for impact-generated porosity and fragmentation have shown that widespread permeable volumes are introduced into the subsurface down to depths of 25 km and at depths of a few km out to 4 crater radii (see Alexander et al., 2024; Marchi et al., 2024).

With these results in mind, a major question that arises is how much of the crust is made permeable—and thereby a possible environment for extremophiles (hydrothermal or lithophytes)—as a result of impacts for the early Earth? This question is the motivation for this study. The goal of this study is to produce a quantitative estimate of the impact induced permeability and investigate to what extent impacts in the Hadean and early Archean introduced permeable regions, which may have played a role in Earth's early pre-biotic evolution, which we explore via a wide parameter space to consider various hypothesized environments and conditions.

2. Methods

Modeling impact-generated permeability on the Archean and Hadean Earth requires an understanding of the structure of the surface and subsurface. However, very few rocks exist on Earth today that are older than 4 billion years (the oldest rocks being from the Acasta gneiss complex, 3.8–4.2 Ga (e.g., Van Kranendonk et al., 2018) and 4.16 Ga metagabbroic intrusions within the Nuvvuagittuq Greenstone Belt, Sole et al., 2025). As a result, our understanding of the environment of the Hadean and Archean is incomplete and limited. Yet, some studies have made estimates for the primitive crustal composition and thickness, heat flow and geothermal gradient, as well as ocean depth (Bickle, 1986; Herzberg et al., 2007; Korenaga, 2021; Sleep & Windley, 1982). From these works, it is generally accepted that the mantle was significantly hotter than today (due to heat from accretion and enrichment of radioactive elements, e.g., Herzberg et al., 2010). Thus, for the early Earth, we explore geothermal gradients of 25, 50 and 75 K/km (with corresponding conductive lid thicknesses of 48.5, 24.2, and 16.1 km depth, respectively). Further, an early basalt crust is expected to overlay the hot mantle, but the thickness of this crust is debated (Korenaga, 2021; O'Neill et al., 2014). To explore the range of possibilities, we simulate 0, 25, 50, and 100 km crustal thicknesses. We also consider the effects of a 5 km ocean overlaying target stratigraphy in select simulations.

All modeling presented in this work was done with a version of the iSALE shock physics code (Amsden et al., 1980; Collins & Melosh, 2014; Collins et al., 2004, 2011; Wünnemann et al., 2006) that includes Grady-Kipp dynamic tensile fragmentation and tensile porosity generation (see Wiggins et al., 2019, 2022). All materials are modeled using the ANEOS equation of state (EoS) for basalt (Wiggins et al., 2022, based on Pierazzo et al. (2005)) and forsterite (based on Benz et al. (1989) and was updated to include molecules and a melt curve by

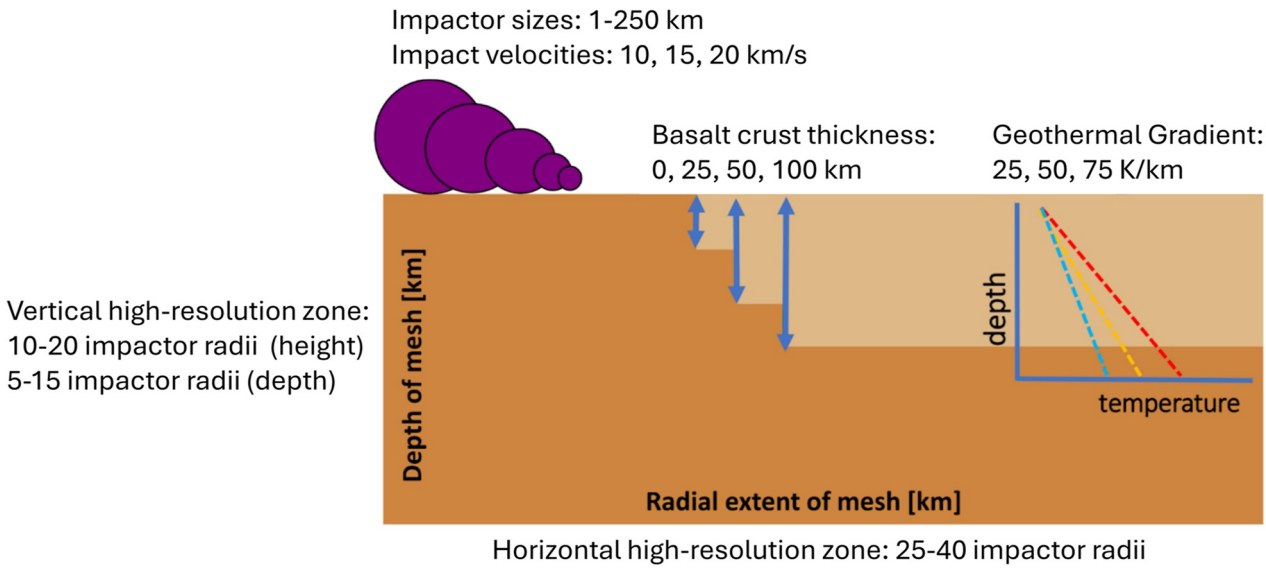

Figure 1. Summary illustration for different impact conditions and Hadean environments explored. We consider impactor sizes 1–250 km in diameter, basalt crust thicknesses 0–100 km thick, geothermal gradients 25–75 K/km. The mesh size is variable based on the impactor size. Ranges of high-resolution zones are depicted. Full mesh sizes ranging from 60 km wide in the smallest case to 26,000 km in the largest case. Not shown are select cases where a 5 km ocean was placed on top of the basalt crust. In total, the results from 37 simulations were analyzed and discussed in this paper. Input files for all simulations can be made available. A full table of all simulations completed is available on Figshare (Alexander et al., 2024).

Collins and Melosh (2014)). For the select few simulations which include an ocean, the Tillotson EoS for water was used (O'Keefe & Ahrens, 1982). We use a strength model suitable for rocky materials (Collins et al., 2004) as well as a dilatancy model to account for porosity generated during shear deformation (Collins & Melosh, 2014). Every simulation has a resolution of 40 cells per projectile radius, which corresponds to a minimum cell size of 12.5, 125, 625, 1,250 and 3,125 m for the 1, 10, 50, 100, and 250 km projectiles, respectively. Each cell within the high resolution zone of our simulation also contains a Lagrangian tracer particle that tracks the motion and state of a parcel of material. An illustration of the full extent of the simulation suite, including mesh sizes, is provided in Figure 1. Material parameters for this modeling can be found in Table S1 in Supporting Information S1. A table of the full simulation suite, with details on mesh and materials are uploaded on FigShare (Alexander, 2026).

Porosity and fracture area are computed, advected, and tracked for each cell and tracer particle numerically via the dilatancy, tensile porosity and tensile fragmentation subroutines mentioned previously. The fragmentation model uses the Weibull parameters λ and m for a specific strain rate ϵ to determine a number of active flaws per unit volume as $N = \lambda\epsilon^m$ following Grady and Kipp (1980). Wiggins et al. (2019) found that for basaltic targets, $\lambda = 10^{36}$ m^{-3} and $m = 9.5$. As described in Wiggins et al. (2019) Appendix A, tensile damage is accumulated when a minimum failure strain is achieved. Fracture area is then computed, advected, and tracked for each cell (see Equation A5, Wiggins et al., 2019) and is used to compute fragment size in post processing as $d_{\text{frag}} = 3(m+3)(m+2)/\text{area}_{\text{frac}}$ where $\text{area}_{\text{frac}}$ is fracture area per unit volume such that fragment size, d_{frag}, has units m. This analytical expression allows for the estimation of permeability introduced by fractures that can be larger than the size of an individual cell.

Permeability is computed following Heap et al. (2020) which computes effective (total) permeability as a two-dimensional model for water flow in parallel layers of a fractured rock mass, from Farquharson and Wadsworth (2018). We modify Heap et al. (2020)'s approach in that permeability due to porosity replaces intact permeability and the permeability due to fracture is an additive quantity per unit volume to the permeability due to porosity yielding Equation 1:

$$k_t = \left(1 - w_f\right) k_p + \left(w_f k_f\right) \tag{1}$$

where w_f is the fractional width of fractures per unit length ($w_f = h/d_{\text{frag}}$), h is average fracture width, set as 0.25×10^{-3} m from the assumptions described in Heap et al. (2020), d_{frag} is the typical fragment size (peak of the

size frequency distribution, computed in iSALE, Wiggins et al., 2019), and $k_f = 1 \times 10^{-9}$ m^2 is the fracture permeability (Heap & Kennedy, 2016; Heap et al., 2020). k_p is the permeability computed from the effect of porosity:

$$k_p = \frac{2\left(1-\left(\phi-\phi_c\right)\left(\phi-\phi_c\right)^n\right)}{\left(-3(1-\phi)\,ln(1-\phi)\right)/a^2} \quad (2)$$

where n is a percolation exponent (set to be 4.4 from Heap et al. (2020)), a is the average pore size (set to be 3.9×10^{-6} m, Alexander et al., 2024), ϕ is the impact-generated porosity which is output from our iSALE modeling and ϕ_c is the percolation threshold (set to be 0.03, Alexander et al., 2024). The numerical values reported here constitute our baseline model, and in Section 4.1 we include a discussion on the selection and effects of these material constants and also perform a sensitive study. We also include a more detailed description of the effective permeability equation (Equation 1) in Section S1 in Supporting Information S1. Permeability, porosity, and fragment size are computed for all unmelted tracer particles. Melted tracers are determined using their peak entropy and pressure (described in detail in Marchi et al. (2026)) and then masked.

3. Results

3.1. Extensive Permeability Is Generated in the Upper Crust

In total, 37 iSALE simulations were conducted to explore the various environments and impact conditions. The "fiducial model" for each impactor size includes an impact velocity of 15 km/s, geothermal gradient of 50 K/km and basalt crust thickness of 50 km. To illustrate the results without including 37 individual crater cross-sections, we show the final permeability through the cratered landscape for each fiducial model of each impactor size in Figure 2. We find that permeable magnitude typically ranges from 10^{-20} to 10^{-12} m^2, as shown by the color bar in Figure 2.

To comment on how these impact-generated permeabilities compare with known terrestrial values, Figure 3, adapted from Ingebritsen and Sanford (1998) and Ingebritsen et al. (2006), shows the permeability generated in this work (yellow shaded bar) relative to other typical permeable thresholds and ranges. From this we impose permeable cut-off of 10^{-20} m^2 where no advective solute transport is expected to occur. All results henceforth will be for permeability greater than 10^{-20} m^2. We note that advective heat transport is expected for permeability greater than 10^{-16} m^2 and we find such permeable conditions are generated for several crater radii beyond the impact point, especially in the upper-most 20 km of the crust.

This permeability is created in the first moments following impact when the material is in tension; minor fluctuations in permeability occur during the rise and collapse of the central uplift (as shown in Figure 4 and Figure S2 in Supporting Information S1).

3.2. Permeability Generation as a Function of Impact Conditions

Next, to show the effects of impact conditions and early Earth environments, permeable volume has been computed for each model for the upper-most 20 km and is shown in Figure 5. The restriction of the uppermost 20 km was imposed as a region with accessible water and where over burden pressure does not immediately crush out voids (see discussion below). The total permeable volume for each simulation is available in the data table uploaded on FigShare (Alexander, 2026).

There is a clear trend of increasing permeable volume with impact energy. This trend is expected, as the stress wave from a higher energy impact penetrates deeper into the crust and further from the impact point, fracturing more material than a lower energy impact. The distribution of all fiducial simulations in the form of impact energy versus permeable volume introduced follows a power law of $V_{\text{perm}} = cE_{\text{imp}}{}^b$ where V_{perm} is the permeable volume generated in km^3 and E_{imp} is the impact energy in Joules. The solid gray line in Figure 5 shows the fit with $c = -12.60 \pm 0.03$ and $b = 0.80 \pm 0.02$, in log-log space. We have also plotted fits for the more conservative permeable thresholds of 10^{-16} m^2 (for heat transport) and 10^{-14} m^2 (typical of modern geothermal reservoirs) in dashed and dotted lines in Figure 5.

10.1029/2025AV002097

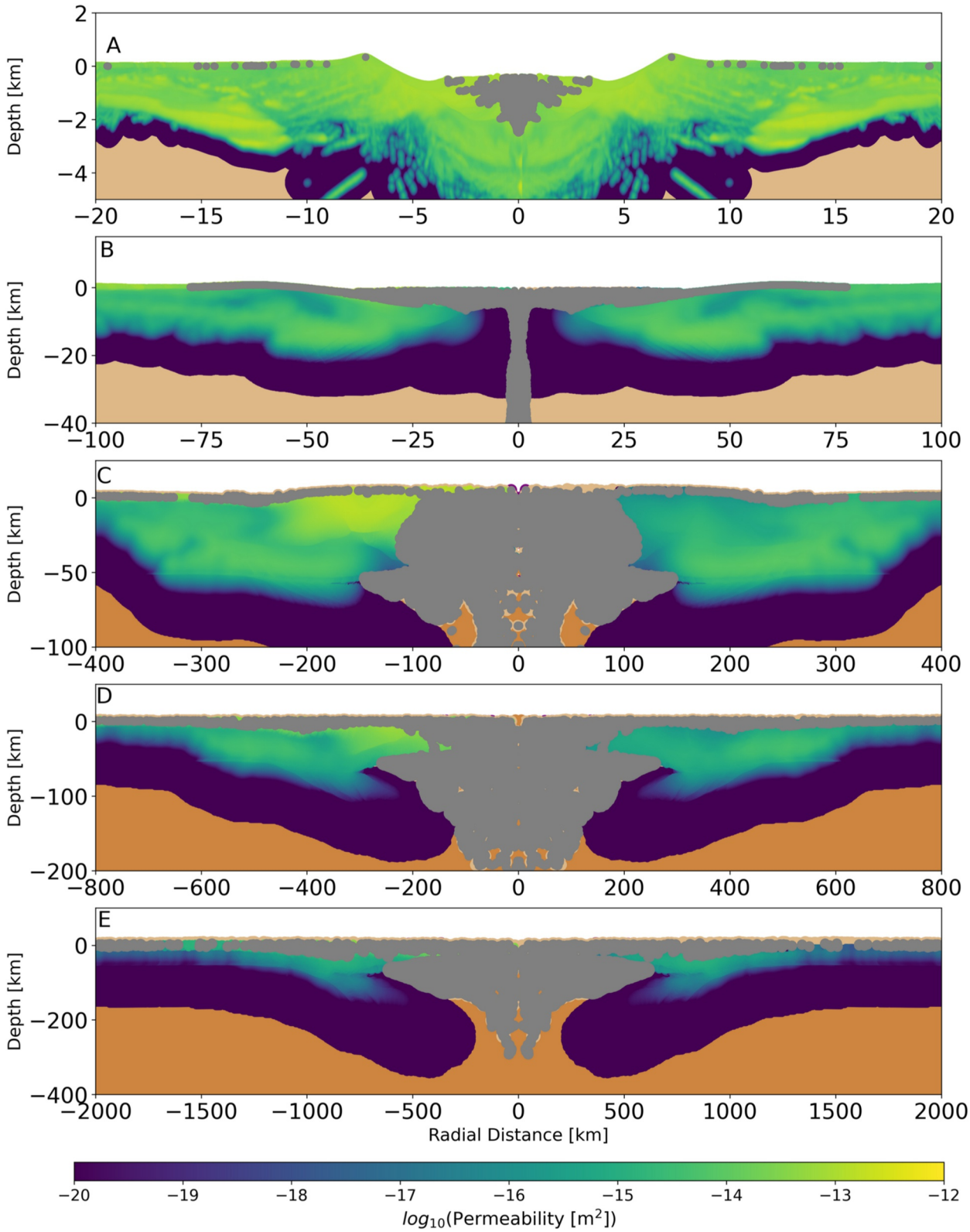

Figure 2.

For comparison, the estimated volume of the modern-day Yellowstone hydrothermal system is $\sim 1 \times 10^4$ km^3 (Kring et al., 2020, show by the yellow "Y" line in Figure 5) and we estimate the volume of impact-generated permeability for Chicxulub as $\sim 1 \times 10^6$ km^3 (Alexander et al., 2024, shown by the blue "C2" line in Figure 5). The 1 km projectile cases generate permeable volumes that are 2–10 times less than the estimated volume for the Yellowstone hydrothermal system. All 10 km impactor cases result in permeable volume similar to what we estimated for the Chicxulub system (Alexander et al., 2024). The 50, 100, and 250 km impactor sizes all generate permeable volumes 2–4 orders of magnitude larger than what we estimated for Chicxulub. We emphasize that even in the most conservative permeable threshold cut-offs, for all impactor sizes, the permeable volume generated by a single impact is greater than the modern Yellowstone hydrothermal system.

Considering environmental parameters, it appears that geothermal gradient, and thickness of a basalt crust do not have a strong effect on the permeable volume, with a scatter up to a factor of 2 relative to the fiducial case (see Figure S3 in Supporting Information S1). The scatter depicted in Figure S3 in Supporting Information S1 is characteristic for all impactor sizes. The total permeable volume for the warmer and cooler geothermal gradient cases (relative to the fiducial) are within ∼10% relative to the fiducial case, while crustal thickness has a wider scatter, corresponding to a variation of up to twice the permeable volume.

The inclusion of a 5 km ocean stunts the development of permeable space. Figure 6 shows the resulting permeability distribution for each of the four cases (1 km, 10 km, 50 km, and 100 km impactors; the 5 km ocean could not be resolved in the 250 km impactor case). When a 5 km ocean is present, the strength of the stress wave from the impact is reduced by passing through the overlying ocean, resulting in less intense and less vast fragmentation. Table 1 quantitatively shows this effect where in each case with an ocean present, there is a ∼30% or less decrease in permeable volume. In addition to reduction in permeable volume, the distribution and magnitude of permeability is different (more permeable)—particularly for the 1 and 10 km impactor cases; permeability magnitude is discussed next.

The magnitude of permeability as a result of impact and environmental conditions can be assessed by looking at the cumulative distribution of permeable values. To do so, we plot the permeability of each tracer particle in the final timestep for each simulation that has permeability $>\sim 10^{-20}$ m^2 and bin them. Figure 7 presents the probability of each permeability (by logarithmic magnitude) within the permeable region in the form of a CDF that is normalized by total permeable volume, for each of the 100-km impactor cases. The CDFs are sorted by impactor size and then colored based on the other model specifics (i.e., impact velocity, target geotherm, basalt crust thickness).

As we imposed the advective solute transport cutoff at 10^{-20} m^{2,} all of the data falls above this threshold. We find that ∼20–50% of the data (depending on impact and environmental conditions) is within the advective heat transport threshold of 10^{-16} m^2 and most of the data is below the modern geothermal reservoir regime of 10^{-14} m^2. Even with the most conservative cut-offs, significant permeable volume is still generated—on the order of 10^3–10^7 km^3, as shown in Figure 3.

From this plot (the trend is similar to the other impactor sizes), we observe that warmer geotherms result in less permeable zones on average while impacts into cooler geotherms lead to regions with overall higher permeability. Pore space generation through shear deformation and dilatancy becomes ineffective when the melt temperature is approached (Collins, 2014). Thus, the enhanced permeability for lower thermal gradients is likely caused by enhanced porosity generation through dilatancy. The presence of an ocean has a similar effect. The increase in temperature with depth is delayed by 5 km, so the stress wave that has already diminished some from the water interacts with cooler material at depth, generating smaller fragments and enhanced porosity generation. Therefore, simulations with the 5 km ocean result in having a higher-than-average permeable magnitude, as compared to the rest of the models (there is a greater volume of material that has permeability $>10^{-14}$ m^2). The effect of the thickness of a basalt crust on permeable magnitude is less obvious, discussed more in the next section.

Figure 2. Final crater cross sections with tracers plotted to show material (light brown = crust, dark brown = mantle; note that both crustal types may not be visible due to overplotted permeability) and permeability (color bar) for each fiducial model run. The colorbar data plotted on left side of each panel represents total permeability from both impact-generated porosity and fragmentation and on the right side of the panel only permeability due to fragmentation is plotted. (a) 1 km impactor; (b) 10 km impactor; (c) 50 km impactor; (d) 100 km impactor; (e) 250 km impactor (all impactors hit a target with 50 km basalt crust, 50 K/km geotherm at 15 km/s). Gray points are melted material, as determined by peak entropy as described in the text. Note that these plots are vertically exaggerated to show the permeable region in detail.

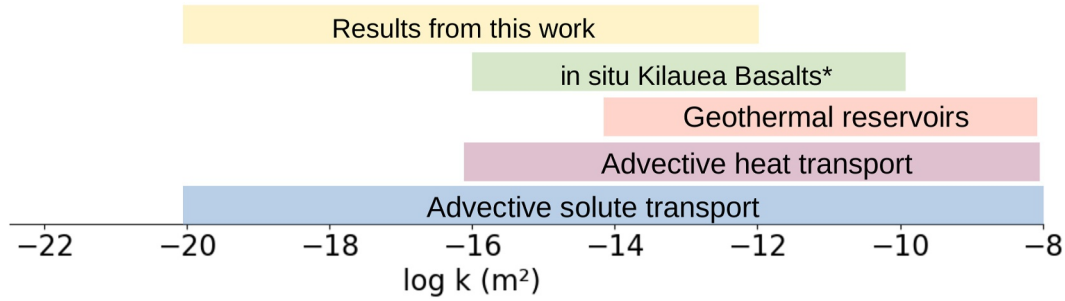

Figure 3. Typical permeability threshold (adapted from Ingebritsen et al. (2006)) for common materials and processes, along with the permeabilities produced in this work. Geothermal reservoirs (sometimes called geothermal fields), such as Yellowstone, are natural underground regions which are porous and permeable with a heat source and groundwater flow.

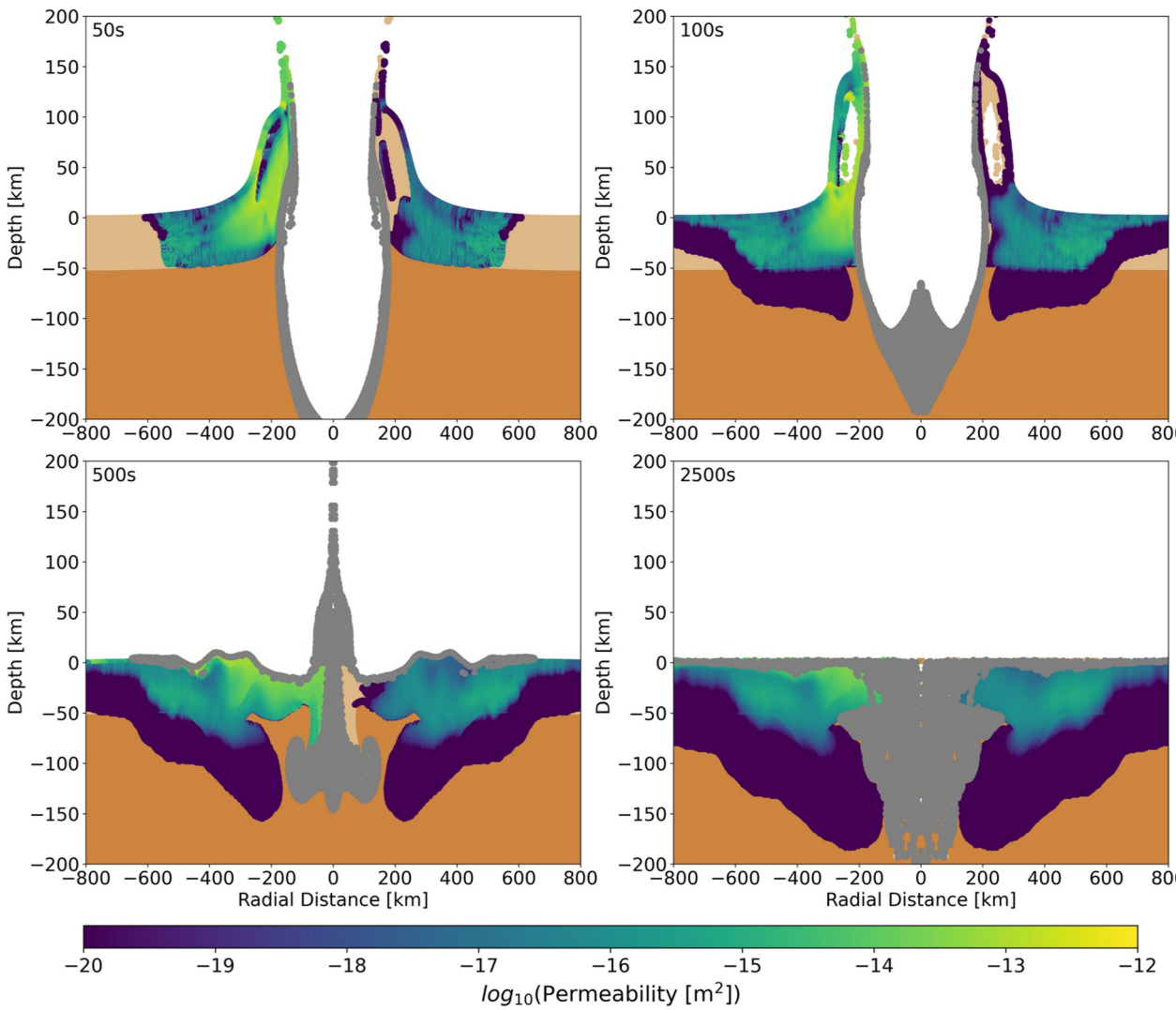

Figure 4. Time series for crater evolution of the fiducial 100 km projectile case. As in Figure 2, tracers plotted with the colorbar represent impact-generated permeability, light brown material represents the basalt crust (although obscured by permeable tracers), dark brown material represents mantle material, and gray tracers represent melted material. Note the axes change between the top two panels and the bottom two panels and that these plots are vertically exaggerated. Note that as in Figure 2, the colorbar data plotted on left side of each panel represents total permeability from both impact-generated porosity and fragmentation and on the right side of the panel only permeability due to fragmentation is plotted.

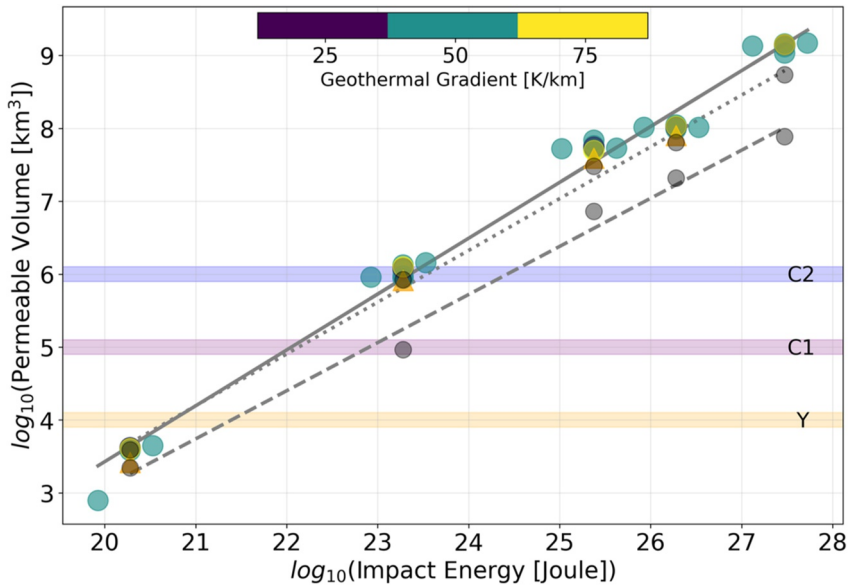

Figure 5. Total permeable volume (for permeability greater than 10^{-20} m^2 and depth less than 20 km) as a function of impact energy. Points are colored based on the simulated geothermal gradient. Orange, triangular points include a 5 km ocean on top of the target stratigraphy for fiducial model set-up. The gray lines (solid, dotted, dashed) are the power law fit for the fiducial models for permeable cutoffs of 10^{-20}, 10^{-16}, 10^{-14} m^2, respectively. Note that individual gray scatter points for each fiducial case at the more conservative permeable thresholds are plotted with their respective lines Line Y = volume estimate for Yellowstone hydrothermal system (Kring et al., 2020); Line C1 = lower volume estimate for Chicxulub impact-generated hydrothermal system (Kring et al., 2020); Line C2 = upper volume estimate for Chicxulub impact-generated hydrothermal system (Alexander et al., 2024).

4. Discussion

The modeling presented in this work is the first comprehensive study of impact-generated permeability for a suite of early Earth crustal environments. In this section we will discuss the nuances of the permeability computation from porosity and fragmentation as well as the effects of material models, parameters and equations of state. Then, we will address limitations and caveats in our approach and calculation. Finally, we will infer implications for recurrent impacts on the early Earth.

4.1. Permeability Distributions and Controls on Permeable Magnitudes

The CDFs of Figure 7 are sorted by impactor size and then colored based on the other model specifics (impact velocity, target geotherm, basalt crust thickness). In general, while impacts with less energy produce overall less permeable volume, the permeability within those regions is higher (i.e., more conducive to fluid flow). This is likely because larger impactors result in larger fragment sizes as compared to smaller impactors (as shown in Figure S4 in Supporting Information S1), due to lower strain rates, yielding a reduced fracture permeability. In addition, larger impactors induce permeability to greater depths, but much of this permeability is low in permeable magnitude.

Another observation is that impacts into the mantle-only models (i.e., 0 km crust) have lower permeable magnitudes than impacts into targets with basalt crust. The permeability computation relies on several material constants (see Alexander et al., 2024) and due to limitations in published works on permeability of impact units, we use the same constants for both basalt and forsterite (from Heap and Kennedy (2016) and Heap et al. (2020) derived for Ries suevites and volcanic andesites). Thus, the difference in permeability between forsterite and basalt in this work must derive from the rheological model parameters and/or the EoS. To determine which, we separate permeability into the components from fragmentation and from porosity (i.e. effective permeability from porosity as $k_\phi = (1 - w_f)\,k_p$) and effective permeability due to fragmentation as $k_{\text{frag}} = w_f k_f$, which are plotted in Figure 8.

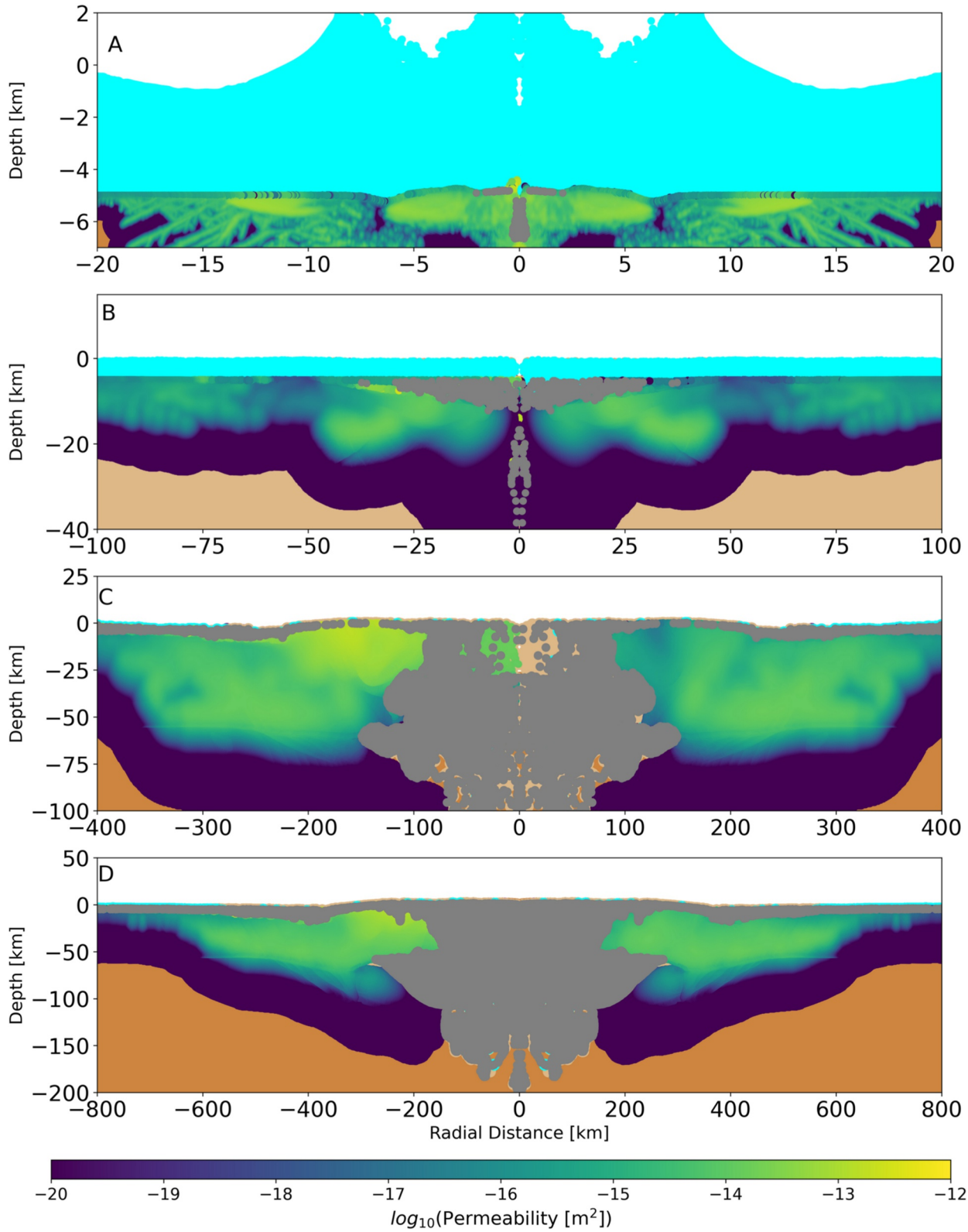

Figure 6.

Comparing the CDFs for permeability from fragmentation and permeability from porosity along with visual inspection of the permeability in the crater cross sections, we find that permeability from fragmentation accounts for the majority of permeable volume (Figure 8d) while permeability from porosity results in higher permeable magnitudes (Figure 8a). That is, fragmentation drives the vast extension of impact-generated permeability, but impact-generated porosity is critical for creating permeable spaces sufficient for fluid flow ($k_t > 10^{-20}$ m^2). In addition, the CDF for permeability from fragmentation alone reveals that the case with no basalt crust has systematically lower permeability than the rest of the models. This reduced permeability is a result of differences in the EoS for forsterite and basalt and how it affects the rarefaction wave; as a result, larger fragments are generated from lower strain rates in the forsterite as compared to basalt.

4.2. Assumptions and Caveats

Computing permeability from porosity and fragmentation is a challenging endeavor that requires several assumptions. Here we detail the basis and limitations of these assumptions. First, as described in Alexander et al. (2024), the fragmentation model implemented by Wiggins et al. (2019), which is used in this work, only accounts for fragmentation as a result of tension. The porosity predicted by material in tension in iSALE is likely an upper bound as this porosity may be compacted out with the rise and collapse of the central uplift and crater modification, but in the model, it is treated as irreversible and persists throughout the simulation. Since our model does not include compaction, the porosity remaining in the final crater is likely an overestimate. As a result, a reduction in permeable magnitude, particularly several crater radii beyond the crater rim, would be reduced. To illustrate this effect in full transparency, the permeability plotted in Figures 2, 4, and 6 shown on the left is always the total permeability including the effects of impact-generated porosity and fragmentation while the right panel is always permeability due to fragmentation alone ($k_{\text{frag}} = w_f k_f$). The differences are subtle as permeability due to fragmentation is the main driver in permeable volume, but permeable magnitude is reduced in parts of the crater when permeability due to porosity is not included.

Second, there is no current model for fragmentation as a result of shearing. Shear fragmentation from the passage of the shock wave as well as during the collapse of the central uplift would result in additional grinding of the material down to smaller fragment sizes. Smaller fragment sizes would subsequently result in higher overall permeability values.

Further, fracture width (h from $w_f = h/d_{\text{frag}}$ from Equation 1) would ideally be calculated as $h = \phi/\text{area}_{\text{frac}}$ where ϕ and $\text{area}_{\text{frac}}$ are both outputs from iSALE. However, due to the lack of shear fragmentation, h computed as such leads only computes the largest fracture widths (greater than meter-scale). While larger fractures would exist, they would be filled in by breccia and cataclasites. Thus, we elect to use $h = 0.25 \times 10^{-3}$ m for our simulation suite from assumptions in Heap et al. (2020). Related, fracture permeability, k_f, would typically be computed as $k_f = h^2/12$ for parallel plates (Zimmerman & Bodvarsson, 1996). However, as we are unable to realistically compute fracture width, we set k_f as a constant for our simulation suite, 1×10^{-9} m^2 (Heap & Kennedy, 2016; Heap et al., 2020).

We caution that effective permeability depends on the scale at which it is observed and calculated. Core data and wellbore data have been shown to have a 3 order of magnitude variation in permeability for crystalline granite but is to the same order of magnitude in tuff and volcanic melt systems (Ingebritsen & Sanford, 1998; Ingebritsen et al., 2006). Heap and Kennedy (2016) similarly cautioned that laboratory measurements of pristine rocks will underestimate the equivalent permeability and that lab measurements of fractured rocks can overestimate the effective permeability. Effective permeability can be computed two-dimensionally for horizontal flow along parallel layers via an arithmetic mean, vertical flow perpendicular to parallel layers via a harmonic mean, and in any random direction from a geometric mean (Baker et al., 2015). In this study, we compute an arithmetic mean of

Figure 6. Final crater cross sections with tracers plotted to show material (light brown = crust, dark brown = mantle, cyan = ocean; note that both crustal types may not be visible due to overplotted permeability) and permeability (color bar) for each fiducial case with an ocean (250 km impactor not shown as it was not modeled as the 5 km ocean could not be resolved). Note: the ocean layer is plotted but not easily visible in panels (c and d). Note that the impact produces a large-scale tsunami and the ocean still sloshes around for long durations post impact (e.g., Range et al., 2022). Eventually, the ocean would return to a steady state, but at longer timescales than the impact simulations are modeled in this work. As in Figures 2 and 4, the colorbar data plotted on left side of each panel represents total permeability from both impact-generated porosity and fragmentation and on the right side of the panel only permeability due to fragmentation is plotted.

Table 1
Permeable Volumes Generated by Impacts for Each of the 1, 10, 50, 100 km Cases With an Ocean and Without

Simulation name with ocean	Permeable volume (km^3)	Simulation name without ocean	Permeable volume (km^3)	Ratio of permeable volumes
1 km fiducial	2.61E+03	1 km fiducial	3.81E+03	0.69
10 km fiducial	8.46E+05	10 km fiducial	1.15E+06	0.74
50 km fiducial	6.14E+07	50 km fiducial	7.33E+07	0.84
100 km fiducial	1.57E+08	100 km fiducial	2.10E+08	0.75

Note. The rightmost column reports the ratio of permeable volume (with ocean:no ocean). The permeable volumes reported here are for the 10^{-20} m^2 permeability cutoff.

the permeability per cell from contributions of each porosity and fragmentation (as introduced in Section 2). For the same set of data, $k_{harm} \leq k_{geom} \leq k_{arith}$ and would only be equal in a homogenous reservoir. Thus, the approach outlined in this work is an upper bound. For more on the computation of arithmetic, geometric, and harmonic effective permeability, see the Section S1 in Supporting Information S1.

4.2.1. Sensitivity of Permeability Computation

We emphasize that petrophysical data for terrestrial impactites is limited. The only known studies which estimate and report the petrophysical constants necessary for computing Equations 1 and 2 have been completed for the Ries impact structure and Chicxulub (both of which are characterized by limestone and granite impactites; reported in Heap et al. (2020) and Alexander et al. (2024), respectively). No known petrophysical constants have

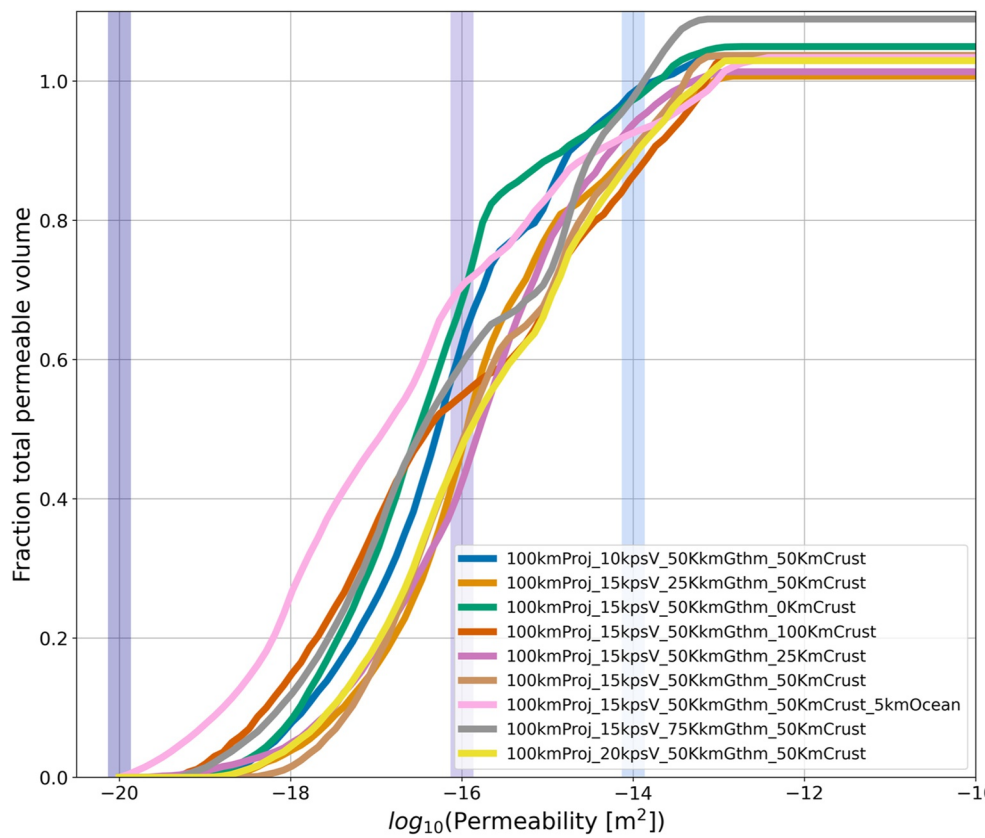

Figure 7. Cumulative distribution functions for permeability within each cell of the mesh that has permeability greater than 1×10^{-20} m^2 and depth > −20 km for the 100 km impactor cases. The *y*-axis represents the fraction of the total permeable volume with permeability less than or equal to the value shown on the *x*-axis; a value of 1 on the *y*-axis corresponds to the entire permeable volume. The purple bars at $\log_{10}k = -20$, −16, and −14 correspond to permeable thresholds for advective solute transport, advective heat transport, and modern geothermal reservoirs, respectively (as described in the text and as illustrated in Figure 3).

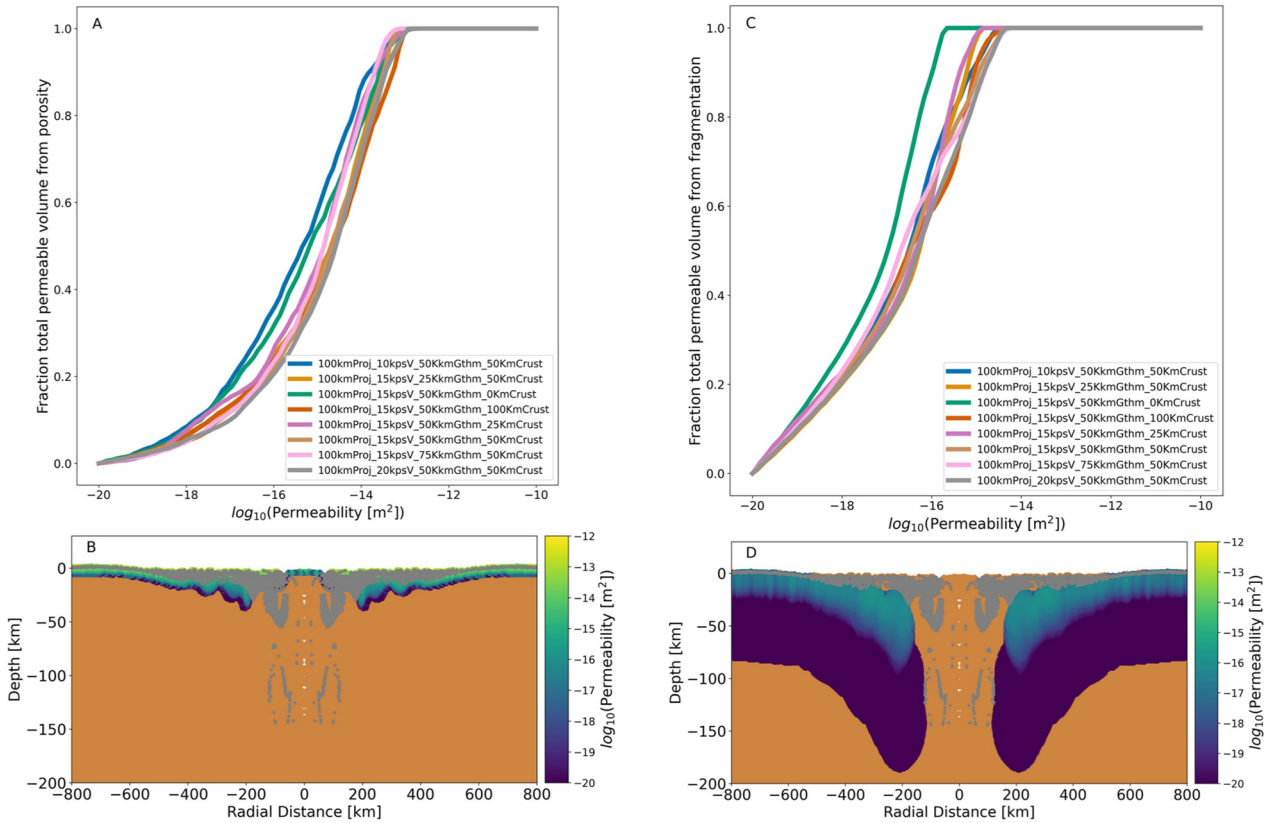

Figure 8. (a) CDF for permeable volume for all 100 km projectile cases where permeability is computed solely from contributions due to impact-generated porosity (permeability $> 10^{-20}$ m^2, depth > -20 km). (b) Crater cross-section for 100 km impactor case and no crust. Tracers with permeability due to porosity only are plotted with the color bar. (c) CDF for permeable volume for all 100 km projectile cases where permeability is computed solely from contributions due to impact-generated fragmentation. (d) Crater cross-section for 100 km impactor case and no crust. Tracers with permeability due to fragmentation only are plotted with the color bar. In both A & D mantle material is shown in dark brown and melt is shown in gray. For all panels, permeability $> 10^{-20}$ m^2, depth > -20 km.

been established for basalt or forsterite targets. Further, the lack of Hadean and early Archean rocks makes it even more difficult to estimate the appropriate constants for this study. To overcome this barrier, we approximate the necessary material constants using those for Chicxulub and Ries. As a result, there may be substantial uncertainties in the resulting porosity and permeability. However, our results from Chicxulub as compared to the drill core suggested impact-generated porosity matched very well and that a ten-factor increase of impact-generated permeable volume could be attributed to large-scale fragmentation not able to be resolved in the drill core data (consistent with findings by Heap and Kennedy (2016)).

To provide assurance that the results of this study are reasonable, we conducted a sensitivity study via monte carlo analysis to vary each material constant in Equations 1 and 2 (i.e., h, n, k_f, a, ϕ_c). The ranges explored (which are obtained from literature) and references for such selections are available in Table S2 in Supporting Information S1. Figure 9 shows the resulting permeable volume histogram and CDFs of realized permeable magnitudes for our study.

This analysis produces a unimodal, right skewed distribution of permeable volume with most realizations clustering around 2.3–2.6 $\times 10^8$ km^3. The volume for the fiducial model (10 km impactor, 15 km/s impact velocity, 50 K/km geotherm, 50 km basalt crust) falls on the lower side of the distribution, approximately 15% below the distribution peak, reflecting our conservative choice of nominal material parameters.

While total permeable volume (regions with $k_t > 10^{-20}$ m^2) varies over a narrow range across the ensemble, permeable magnitude exhibits greater variability. Specifically, the median permeability magnitude spans several orders of magnitude across the 1,000 realizations, despite falling well within the 5th to 95th percentile range of the explored parameter space. This indicates that while the extent of permeability generated by impact processes is

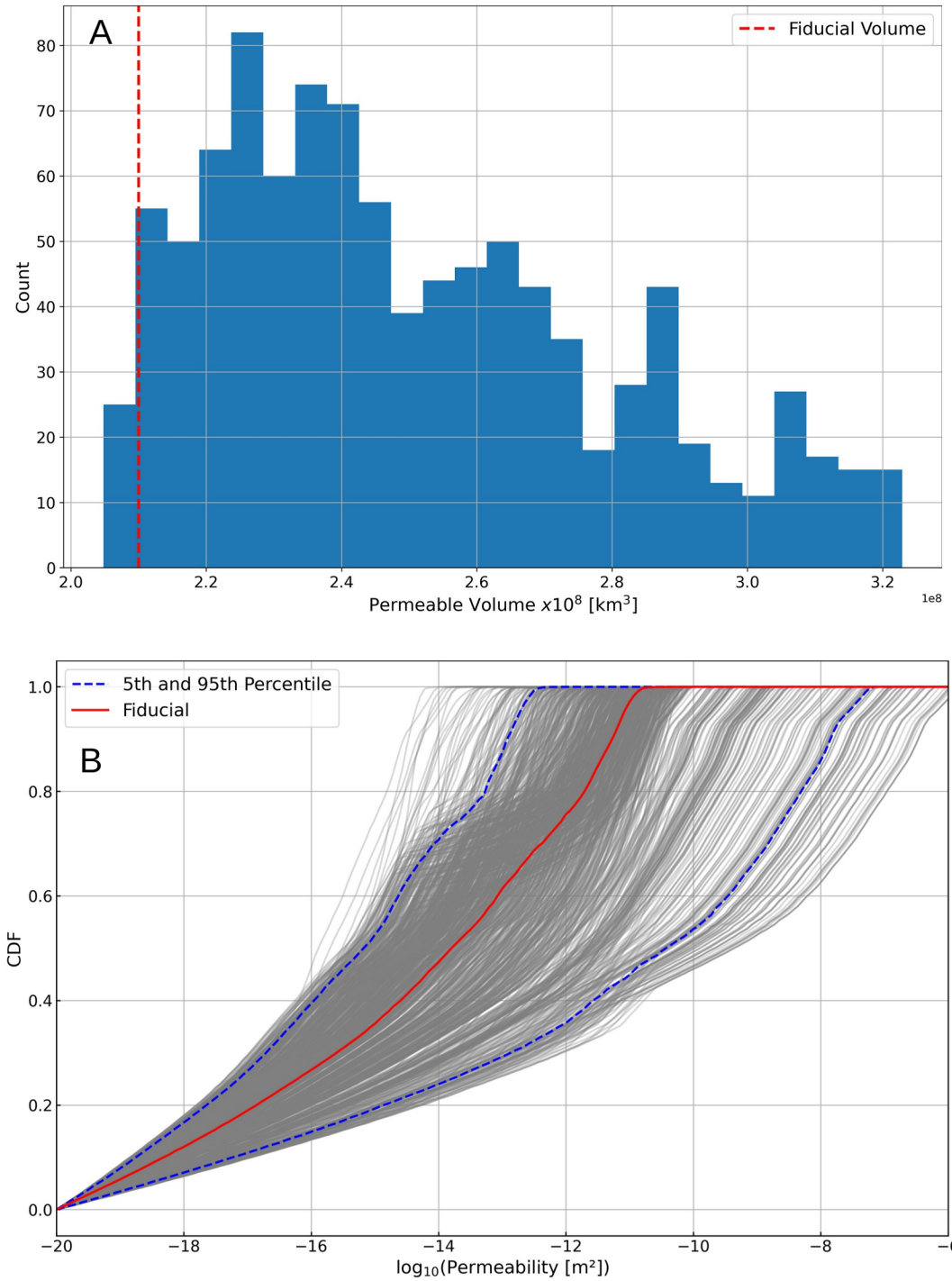

Figure 9. Results from sensitivity analysis for permeability computation. (a) Histogram of permeable volume for each parameter arrangement (i.e., h, n, k_f, a, ϕ_c) in our study (n = 1,000). The red dotted line is the total permeable volume computed for the fiducial 100 km impactor case. (b) All permeable CDFs for each parameter arrangement in our study are shown in gray. The red line is the CDF for the fiducial 100 km case, which matches the brown curve in Figure 7. The blue dashed lines show the 5th and 95th percentiles (see text for details).

robust to uncertainties in the material parameters, the intensity of permeability is more sensitive to those same parameters. We find that uncertainty around the fracture constants (specifically h and subsequently k_f) have the strongest influence on permeable volume magnitude (see Figure S7 in Supporting Information S1).

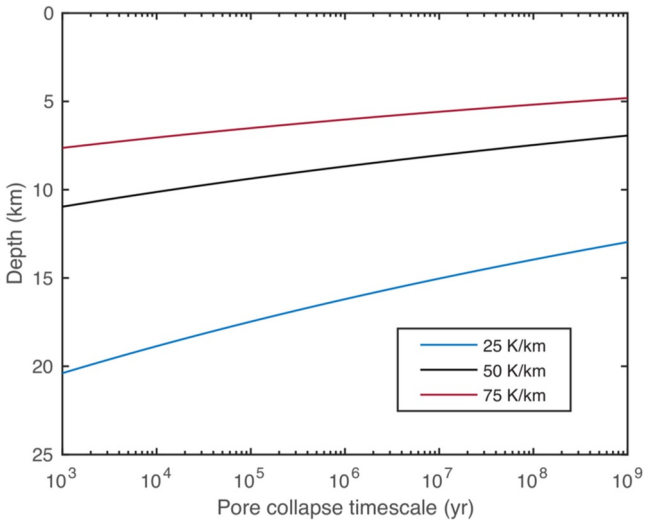

Figure 10. Timescale for pore collapse as a function of depth (overburden pressure and temperature) for each geothermal gradient used in our simulations.

Another complicating factor would be preexisting target rock permeability. Heap and Kennedy (2016) found that for a host rock with very high pre-impact permeability (10^{-12} to 10^{-11} m^2), the presence of tensile fractures did not raise the permeability. However in their tests for rocks with low permeability ($<10^{-15}$ m^2), tensile fractures increase the permeability by several orders of magnitude. In this work we assume intact rock, but find that permeability values converge to a maximum of $\sim10^{-12}$ m^2, which is in agreement with the limit for pre-fractured rock. Further, rock with permeability $>10^{-15}$ m^2 would likely be limited to the uppermost surface as the lifetime for voids and fractures is limited by overburden pressure.

4.2.2. Closure of Void Space

Due to the closure of pores and fractures as a consequence of overburden pressure (Fowler, 1985; Nara et al., 2011), which is complicated by heat flow and fluid flux, there is also uncertainty in the lifetime of the permeable region at depth. We show a simple conceptualization of the lifetime of the permeable region (not accounting for fluid flow, impact heating or cooling, or mineralization) in Figure 10, we consider the viscous closure of void space. The longevity of the permeable regions can be described as a function of the overburden pressure (Fowler, 1985). Figure 10 shows the closure timescale for voids with depth for the relevant geothermal gradients calculated using the flow law for Maryland diabase (Caristan, 1982). Note that diabase is an intrusive igneous rock with a basaltic composition and should be a reasonable analog for the crust. The timescales depicted in Figure 10 are relevant far from the impact point, where impact heating is minimal and significant permeability present (e.g., several crater radii away, in the upper-most 20 km; see Figure 2).

If we consider that the lifetime for the Chicxulub hydrothermal system is estimated to be at least 10^6 years (Kring et al., 2020), we find that the fractures and pores generated by impact which survive more than 10^6 years would be confined to depths of ~18, 10, and 7 km for geotherms 25, 50, and 75 K/km, respectively. Thus, long-lasting permeability would be restricted to the upper crust. It is worth noting, however, that the estimated lifetime of Chicxulub's hydrothermal system neglects the effect of pore closure. Closer to the melt sheet, it is harder to estimate the lifetime of voids due to competing processes expediting (i.e., impact heating) and delaying (fluid flow) closure.

4.3. Broader Implications for the Early Earth

The early Earth experienced frequent bombardment during the Archean and Hadean eons. The findings from this study emphasize that each impact would have imparted significant permeable space into the upper crust. Using a characteristic impact flux for the early Earth produced by monte carlo modeling in Marchi et al. (2021), we compute the incremental impact-generated permeable volume for the early Earth (Figure 11). The figure shows an incremental plot of total permeable volume (which may be contributed from multiple concurrent but not overlapping impacts) for that time bin. Note that we do not assume overlapping impacts (i.e., concurrent and subsequent impacts are impacting an intact surface), nor do we include void closure in this model.

From this plot, for all times where the orange envelope exceeds the gray dashed line, the entire upper 20 km of the Earth's crust would have been permeable. As void closure is neglected in our model, we also consider the effect of impact injected permeability in the upper 8 km of the crust, where void closure can be neglected since the collapse timescale is greater than the 25 Myr time bin for the nominal geothermal gradient of 50 K/km. There is a vertical shift in the envelope, shown in the red outline in Figure 9, illustrating the decrease in permeable volume due to a smaller volume of crust being considered.

Prior to 4.3 Ga, both the 8 and 20 km shells are repeatedly made permeable at any time bin. By 4.25 and 4.1 Ga, the permeable volume drops below saturation for 20 and 8 km, respectively. Significant impact-generated permeability (>50% shell volume) in the upper 8 and 20 km remains until about 3.75 and 3.8 Ga, respectively. The system reaches steady state by ~3.5 Ga where occasional large impacts boost permeability on a local scale. In all time bins, the permeability introduced by impacts exceeds the size of the modern Yellowstone geothermal system

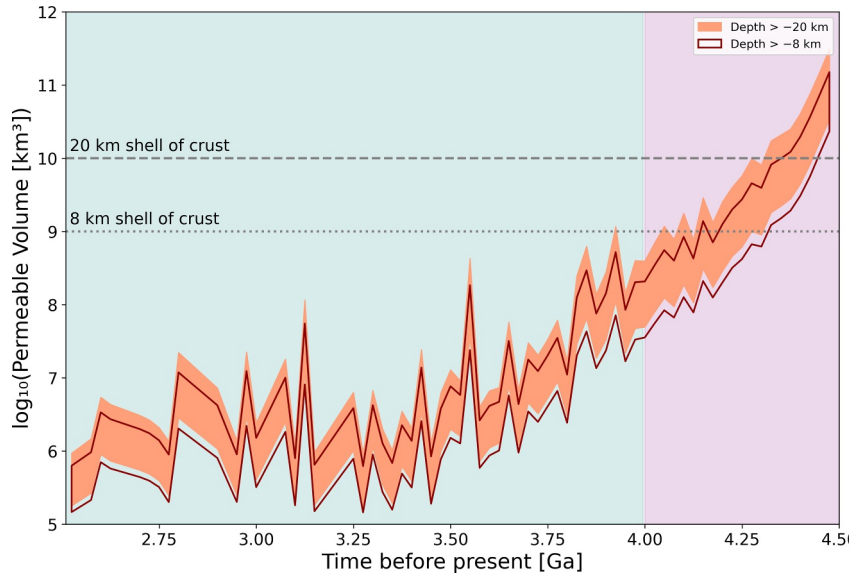

Figure 11. Incremental permeable volume introduced into the upper crust (less than 8 km deep shown in red which is the contour of the envelope of data and less than 20 km deep is shown as the solid orange envelope) on the early Earth. The top of each envelope represents permeable volume for a permeable threshold of 10^{-20} m^2 while the lower most data represents the permeable volume for a permeable threshold of 10^{-14} m^2. The blue shaded region in the background represents the Archean Eon; the purple shaded background region represents the Hadean Eon. Each time bin is equal to 25 Mya.

($\sim 10^4$ km^3). These permeable systems can be destroyed by subsequent overlapping impacts (which do not occur in this model), but the lifetime of such systems is estimated to be up to $\sim 10^6$ years for impactors $\sim$10 km in size (see Marchi et al., 2024 for an estimation for Vredefort and Abramov and Kring (2007), for an estimate based on Chicxulub). Thus, it is likely that the near-surface portion of such systems thrived before the next impact hit the same location. Furthermore, the permeability in the upper 8 and 20 km of the early Earth would have had a more uniform distribution as compared to the observed exponential decay of permeability in the modern crust.

5. Conclusion

The Hadean and early Archean was a tumultuous time governed by a hotter planet with a primitive basaltic crust that was continuously bombarded by planetesimals and asteroids. In this paper, we present the first extensive and exploratory study on the effects of recursive impacts with respect to the surface and subsurface of the early Earth. Such impacts fracture the crust and generate vast regions of permeability. Inferences from our suite of impact simulations suggest that the volume of impact-induced permeable regions is strongly dependent on impact energy (i.e., impactor size and velocity). The magnitude of the permeability within those regions, however, depends on the geothermal gradient (due to more porosity generation via dilatancy and more fracturing due to reduced ductility for cooler thermal profiles) and composition (due to increased fragmentation as a result of material differences in the equations of state interacting with the rarefaction wave). Coupling these permeability estimates with a characteristic impact flux for the early Earth, we find that the entirety of the uppermost 8 and 20 km of the crust is repeatedly made permeable in the first half of the Hadean and drops below 50% of the shell volume by the early Archean. These shallow permeable networks generated by recursive impacts during the Hadean may have served as crucibles for prebiotic chemistry.

Conflict of Interest

The authors declare no conflicts of interest relevant to this study.

Availability Statement

Input files for our models as well as a data table, complete with simulation and mesh set up and resulting permeable volumes are on FigShare (Alexander, 2026).

Acknowledgments
This work was funded by the NASA Habitable Worlds program (80NSSC21K1798), the NASA ExoBiology program (80NSSC23K0317) and NASA SSERVI (80NSSC23M0176). We gratefully acknowledge the developers of iSALE-2D, including Gareth Collins, Kai Wünnemann, Dirk Elbeshausen, Tom Davison, Boris Ivanov and Jay Melosh. We thank two anonymous reviewers as well as Gareth Collins and Bob Grimm for their revisions, suggestions, and guidance in more accurately computing permeability and representing the limitations due to scale and iSALE subroutines.

References

Abramov, O., & Kring, D. A. (2005). Impact-induced hydrothermal activity on early Mars. *Journal of Geophysical Research*, *110*(E12), E12S09. https://doi.org/10.1029/2005JE002453

Abramov, O., & Kring, D. A. (2007). Numerical modeling of impact-induced hydrothermal activity at the Chicxulub crater. *Meteoritics & Planetary Science*, *42*(1), 93–112. https://doi.org/10.1111/j.1945-5100.2007.tb00220.x

Abramov, O., Kring, D. A., & Mojzsis, S. J. (2013). The impact environment of the Hadean Earth. *Geochemistry*, *73*(3), 227–248. https://doi.org/10.1016/j.chemer.2013.08.004

Abramov, O., & Mojzsis, S. J. (2009). Microbial habitability of the Hadean Earth during the late heavy bombardment. *Nature*, *459*(7245), 419–422. https://doi.org/10.1038/nature08015

Alexander, A. M. (2026). Data for "Widespread Impact-Induced Crustal Permeability on the Early Earth" [Dataset]. *figshare*. https://doi.org/10.6084/m9.figshare.28516202.v1

Alexander, A. M., Marchi, S., Johnson, B. C., Wiggins, S. E., & Kring, D. A. (2024). Impact-generated fragmentation, porosity, and permeability within the Chicxulub impact structure. *Earth and Space Science*, *11*(5), e2023EA003383. https://doi.org/10.1029/2023EA003383

Amsden, A. A., Ruppel, H. M., & Hirt, C. W. (1980). *SALE: A simplified ALE computer program for fluid flow at all speeds* (No. LA-8095). Los Alamos National Lab. (LANL). https://doi.org/10.2172/5176006

Baker, R. O., Yarranton, H. W., & Jensen, J. L. (2015). Reservoir characterization methods. In *Practical reservoir engineering and characterization* (pp. 349–434). Gulf Professional Publishing. https://doi.org/10.1016/B978-0-12-801811-8.00010-9

Benz, W., Cameron, A. G. W., & Melosh, H. J. (1989). The origin of the Moon and the single-impact hypothesis III. *Icarus*, *81*(1), 113–131. https://doi.org/10.1016/0019-1035(89)90129-2

Bickle, M. J. (1986). Implications of melting for stabilisation of the lithosphere and heat loss in the Archaean. *Earth and Planetary Science Letters*, *80*(3–4), 314–324. https://doi.org/10.1016/0012-821X(86)90113-5

Brasser, R., Werner, S. C., & Mojzsis, S. J. (2020). Impact bombardment chronology of the terrestrial planets from 4.5 Ga to 3.5 Ga. *Icarus*, *338*, 113514. https://doi.org/10.1016/j.icarus.2019.113514

Caristan, Y. (1982). The transition from high temperature creep to fracture in Maryland diabase. *Journal of Geophysical Research*, *87*(B8), 6781–6790. https://doi.org/10.1029/JB087iB08p06781

Cockell, C. S., Collins, G. S., Basu, S., Grant, E., & McMahon, S. (2024). Martian impact fracturing pervasively influences habitability. *Journal of Geophysical Research: Planets*, *129*(9), e2023JE008116. https://doi.org/10.1029/2023JE008116

Cockell, C. S., Lee, P., Broady, P., Lim, D. S. S., Osinski, G. R., Parnell, J., et al. (2005). Effects of asteroid and comet impacts on habitats for lithophytic organisms—A synthesis. *Meteoritics & Planetary Science*, *40*(12), 1901–1914. https://doi.org/10.1111/j.1945-5100.2005.tb00153.x

Collins, G. S. (2014). Numerical simulations of impact crater formation with dilatancy. *Journal of Geophysical Research: Planets*, *119*(12), 2600–2619. https://doi.org/10.1002/2014JE004708

Collins, G. S., & Melosh, H. J. (2014). Improvements to ANEOS for multiple phase transitions. In *Lunar planet. sci. conf* (Vol. 45, p. 2664).

Collins, G. S., Melosh, H. J., & Ivanov, B. A. (2004). Modeling damage and deformation in impact simulations. *Meteoritics & Planetary Science*, *39*(2), 217–231. https://doi.org/10.1111/j.1945-5100.2004.tb00337.x

Collins, G. S., Melosh, H. J., & Wünnemann, K. (2011). Improvements to the ε-α porous compaction model for simulating impacts into high-porosity solar system objects. *International Journal of Impact Engineering*, *38*(6), 434–439. https://doi.org/10.1016/j.ijimpeng.2010.10.013

Farquharson, J. I., & Wadsworth, F. B. (2018). Upscaling permeability in anisotropic volcanic systems. *Journal of Volcanology and Geothermal Research*, *364*, 35–47. https://doi.org/10.1016/j.jvolgeores.2018.09.002

Fowler, A. C. (1985). A mathematical model of magma transport in the asthenosphere. *Geophysical & Astrophysical Fluid Dynamics*, *33*(1–4), 63–96. https://doi.org/10.1080/03091928508245423

Grady, D. E., & Kipp, M. E. (1980). Continuum modelling of explosive fracture in oil shale. *International Journal of Rock Mechanics and Mining Sciences & Geomechanics Abstracts*, *17*(3), 147–157. https://doi.org/10.1016/0148-9062(80)91361-3

Grimm, R. E., & Marchi, S. (2018). Direct thermal effects of the Hadean bombardment did not limit early subsurface habitability. *Earth and Planetary Science Letters*, *485*, 1–8. https://doi.org/10.1016/j.epsl.2017.12.043

Heap, M. J., Gilg, H. A., Byrne, P. K., Wadsworth, F. B., & Reuschlé, T. (2020). Petrophysical properties, mechanical behaviour, and failure modes of impact melt-bearing breccia (suevite) from the Ries impact crater (Germany). *Icarus*, *349*, 113873. https://doi.org/10.1016/j.icarus.2020.113873

Heap, M. J., & Kennedy, B. M. (2016). Exploring the scale-dependent permeability of fractured andesite. *Earth and Planetary Science Letters*, *447*, 139–150. https://doi.org/10.1016/j.epsl.2016.05.004

Herzberg, C., Asimow, P. D., Arndt, N., Niu, Y., Lesher, C. M., Fitton, J. G., et al. (2007). Temperatures in ambient mantle and plumes: Constraints from basalts, picrites, and komatiites. *Geochemistry, Geophysics, Geosystems*, *8*(2). https://doi.org/10.1029/2006GC001390

Herzberg, C., Condie, K., & Korenaga, J. (2010). Thermal history of the Earth and its petrological expression. *Earth and Planetary Science Letters*, *292*(1–2), 79–88. https://doi.org/10.1016/j.epsl.2010.01.022

Ingebritsen, S. E., & Sanford, W. E. (1998). *Groundwater in geologic processes* (1st ed.). Cambridge University Press.

Ingebritsen, S. E., Sanford, W. E., & Neuzil, C. E. (2006). *Groundwater in geologic processes* (2nd ed.). Cambridge University Press.

Johnson, B. C., Collins, G. S., Minton, D. A., Bowling, T. J., Simonson, B. M., & Zuber, M. T. (2016). Spherule layers, crater scaling laws, and the population of ancient terrestrial impactors. *Icarus*, *271*, 350–359. https://doi.org/10.1016/j.icarus.2016.02.023

Johnson, B. C., & Melosh, H. J. (2012). Impact spherules as a record of an ancient heavy bombardment of Earth. *Nature*, *485*(7396), 75–77. https://doi.org/10.1038/nature10982

Kirsimäe, K., & Osinski, G. R. (2012). Impact-induced hydrothermal activity. In *Impact cratering* (pp. 76–89). John Wiley & Sons, Ltd. https://doi.org/10.1002/9781118447307.ch6

Korenaga, J. (2021). Hadean geodynamics and the nature of early continental crust. *Precambrian Research*, *359*, 106178. https://doi.org/10.1016/j.precamres.2021.106178

Kring, D. A., Tikoo, S. M., Schmieder, M., Riller, U., Rebolledo-Vieyra, M., Simpson, S. L., et al. (2020). Probing the hydrothermal system of the Chicxulub impact crater. *Science Advances*, *6*(22), eaaz3053. https://doi.org/10.1126/sciadv.aaz3053

Longo, A., & Damer, B. (2020). Factoring origin of life hypotheses into the search for life in the solar system and beyond. *Life*, *10*(5), 52. https://doi.org/10.3390/life10050052

Marchi, S., Alexander, A., Trowbridge, A., & Koeberl, C. (2024). Impact-generated permeability and hydrothermal circulation at the Vredefort impact structure, South Africa. *Earth and Space Science*, *11*(1), e2023EA003065. https://doi.org/10.1029/2023EA003065

Marchi, S., Alexander, A. M., Citron, R., & Johnson, B. C. (2026). Impact-generated mixing, melting and vaporization of the early Earth's crust. *Earth and Space Science*, *13*(2), e2025EA004364. https://doi.org/10.1029/2025EA004364

Marchi, S., Bottke, W. F., Elkins-Tanton, L. T., Bierhaus, M., Wuennemann, K., Morbidelli, A., & Kring, D. A. (2014). Widespread mixing and burial of Earth's Hadean crust by asteroid impacts. *Nature*, *511*(7511), 578–582. https://doi.org/10.1038/nature13539

Marchi, S., Bottke, W. F., Kring, D. A., & Morbidelli, A. (2012). The onset of the lunar cataclysm as recorded in its ancient crater populations. *Earth and Planetary Science Letters*, *325–326*, 27–38. https://doi.org/10.1016/j.epsl.2012.01.021

Marchi, S., Drabon, N., Schulz, T., Schaefer, L., Nesvorny, D., Bottke, W. F., et al. (2021). Delayed and variable late Archaean atmospheric oxidation due to high collision rates on Earth. *Nature Geoscience*, *14*(11), 827–831. https://doi.org/10.1038/s41561-021-00835-9

Marchi, S., Mottola, S., Cremonese, G., Massironi, M., & Martellato, E. (2009). A new chronology for the Moon and Mercury. *The Astronomical Journal*, *137*(6), 4936–4948. https://doi.org/10.1088/0004-6256/137/6/4936

Martin, W., Baross, J., Kelley, D., & Russell, M. J. (2008). Hydrothermal vents and the origin of life. *Nature Reviews Microbiology*, *6*(11), 805–814. https://doi.org/10.1038/nrmicro1991

Mojzsis, S. J., Brasser, R., Kelly, N. M., Abramov, O., & Werner, S. C. (2019). Onset of giant planet migration before 4480 million years ago. *The Astrophysical Journal*, *881*(1), 44. https://doi.org/10.3847/1538-4357/ab2c03

Morbidelli, A., Marchi, S., Bottke, W. F., & Kring, D. A. (2012). A sawtooth-like timeline for the first billion years of lunar bombardment. *Earth and Planetary Science Letters*, *355–356*, 144–151. https://doi.org/10.1016/j.epsl.2012.07.037

Morbidelli, A., Nesvorny, D., Laurenz, V., Marchi, S., Rubie, D. C., Elkins-Tanton, L., et al. (2018). The timeline of the lunar bombardment: Revisited. *Icarus*, *305*, 262–276. https://doi.org/10.1016/j.icarus.2017.12.046

Nara, Y., Meredith, P. G., Yoneda, T., & Kaneko, K. (2011). Influence of macro-fractures and micro-fractures on permeability and elastic wave velocities in basalt at elevated pressure. *Tectonophysics*, *503*(1–2), 52–59. https://doi.org/10.1016/j.tecto.2010.09.027

Nesvorný, D., Roig, F. V., Vokrouhlický, D., Bottke, W. F., Marchi, S., Morbidelli, A., & Deienno, R. (2023). Early bombardment of the moon: Connecting the lunar crater record to the terrestrial planet formation. *Icarus*, *399*, 115545. https://doi.org/10.1016/j.icarus.2023.115545

Neukum, G. (1984). Meteorite bombardment and dating of planetary surfaces.

O'Keefe, J. D., & Ahrens, T. J. (1982). The interaction of the Cretaceous/Tertiary Extinction Bolide with the atmosphere, ocean, and solid Earth. In L. T. Silver & P. H. Schultz (Eds.), *Geological implications of impacts of large asteroids and comets on the Earth*. Geological Society of America. https://doi.org/10.1130/SPE190-p103

O'Neill, C., Marchi, S., Zhang, S., & Bottke, W. (2014). Impact-driven subduction on the Hadean Earth. *Nature Geoscience*, *10*, 793–797. https://doi.org/10.1038/ngeo3029

Osinski, G. R., Cockell, C. S., Pontefract, A., & Sapers, H. M. (2020). The role of meteorite impacts in the origin of life. *Astrobiology*, *20*(9), 1121–1149. https://doi.org/10.1089/ast.2019.2203

Osinski, G. R., Tornabene, L. L., Banerjee, N. R., Cockell, C. S., Flemming, R., Izawa, M. R. M., et al. (2013). Impact-generated hydrothermal systems on Earth and Mars. *Icarus, Terrestrial Analogs for Mars: Mars Science Laboratory and Beyond*, *224*(2), 347–363. https://doi.org/10.1016/j.icarus.2012.08.030

Pierazzo, E., Artemieva, N. A., & Ivanov, B. A. (2005). Starting conditions for hydrothermal systems underneath Martian craters: Hydrocode modeling. In T. Kenkmann, F. Hörz, & A. Deutsch (Eds.), *Large meteorite impacts III*. Geological Society of America. https://doi.org/10.1130/0-8137-2384-1.443

Range, M. M., Arbic, B. K., Johnson, B. C., Moore, T. C., Titov, V., Adcroft, A. J., et al. (2022). The Chicxulub impact produced a powerful global tsunami. *AGU Advances*, *3*(5), e2021AV000627. https://doi.org/10.1029/2021AV000627

Robbins, S. J. (2014). New crater calibrations for the lunar crater-age chronology. *Earth and Planetary Science Letters*, *403*, 188–198. https://doi.org/10.1016/j.epsl.2014.06.038

Sleep, N. H., & Windley, B. F. (1982). Archean plate tectonics: Constraints and inferences. *The Journal of Geology*, *90*(4), 363–379. https://doi.org/10.1086/628691

Sole, C., O'neil, J., Rizo, H., Paquette, J. L., Benn, D., & Plakholm, J. (2025). Evidence for Hadean mafic intrusions in the Nuvvuagittuq Greenstone Belt, Canada. *Science*, *388*(6754), 1431–1435. https://doi.org/10.1126/science.ads8461

Trowbridge, A. J., Marchi, S., Osinski, G. R., & Taron, J. M. (2024). Modeling of the impact-generated hydrothermal system at the Haughton impact structure. *Journal of Geophysical Research: Planets*, *129*(7), e2023JE008267. https://doi.org/10.1029/2023JE008267

Van Kranendonk, M. J., Bennett, V., & Hoffmann, E. (2018). *Earth's oldest rocks*. Elsevier.

Wiggins, S. E., Johnson, B. C., Bowling, T. J., Melosh, H. J., & Silber, E. A. (2019). Impact fragmentation and the development of the deep lunar megaregolith. *Journal of Geophysical Research: Planets*, *124*(4), 941–957. https://doi.org/10.1029/2018JE005757

Wiggins, S. E., Johnson, B. C., Collins, G. S., Jay Melosh, H., & Marchi, S. (2022). Widespread impact-generated porosity in early planetary crusts. *Nature Communications*, *13*(1), 4817. https://doi.org/10.1038/s41467-022-32445-3

Wünnemann, K., Collins, G. S., & Melosh, H. J. (2006). A strain-based porosity model for use in hydrocode simulations of impacts and implications for transient crater growth in porous targets. *Icarus*, *180*(2), 514–527. https://doi.org/10.1016/j.icarus.2005.10.013

Zimmerman, R. W., & Bodvarsson, G. S. (1996). Hydraulic conductivity of rock fractures. *Transport in Porous Media*, *23*, 1–30. https://doi.org/10.1007/BF00145263